Influence of temperature and point defects on the X-ray diffraction pattern of graphite

Carbon Trends 5 (2021) 100124

Contents lists available at ScienceDirect

Carbon Trends

journal homepage: www.elsevier.com/locate/cartre

Influence of temperature and point defects on the X-ray diffraction pattern of graphite

Rhiannon Phillips[a], Kenny Jolley[a,*], Ying Zhou[a], Roger Smith[a,b]

[a] School of Science, Loughborough University, Loughborough, LE11 3TU, UK
[b] Laboratory of Nanoelectronics and Nanophotonics, Tomsk State University, Lenin Ave, 36, Tomsk, 634050, Russia

ARTICLE INFO

Article history:
Received 17 August 2021
Revised 22 October 2021
Accepted 25 October 2021

Keywords:
Graphite
Neutron irradiation damage
X-Ray diffraction
Lattice parameter
Interstitials
Vacancies
Reaxff

ABSTRACT

The atomic structure of pure and defective graphite has been modelled using classical many body potentials from which simulated powder X-ray Diffraction (XRD) patterns were produced using the Debyer software. The changes in the XRD patterns due to both heating and the inclusion of defects were investigated. After heating, the results show a shift in the 004 Laue peak in qualitative agreement with experiment. The *c* parameter is shown to increase over the temperature range 0 – 1000 K but there is a slight reduction in the *a* parameter over this range. The scattering angle for the 004 peak reduces with the introduction of defects up to ≈ 5% defect concentration for both vacancies and interstitials with a larger reduction in the case of interstitials. The intensity of the scattering peak is reduced with increasing interstitials (25% reduction at 5% concentration), but remains relatively constant with increasing vacancies. The introduction of a small percentage of interstitials causes an increase in both the *a* and *c* parameters but vacancies cause a reduction in the *a* parameter.

1. Introduction

Several types of existing nuclear reactors (for example, the UK's Advanced Gas-cooled Reactors (AGRs)) use graphite as a moderator, due to its low atomic mass and high scattering cross section [1,2]. Graphite has a high melting point enabling it to withstand the extreme temperatures within a reactor, making it ideal for use in next-generation High Temperature Gas-Cooled Reactors (HTGRs) [3–5].

Given that the lifetime of these nuclear reactors is limited mainly by the level of deterioration in the structure of the graphite, to ensure the safe operation and maximise power output, it is necessary to be able to predict the changes induced in the material over long term irradiation, and to manage their effects [1,6].

Pristine graphite is composed of layers of graphene sheets in which the carbon atoms are arranged in an hexagonal structure. These graphene sheets are generally found in one of three positions *A*, *B* and *C*, which differ from each other by a translation of one carbon-carbon bond length in the armchair (or $\langle 10\bar{1}0 \rangle$) direction. In graphite the layers are generally ordered in an *ABAB* Bernal-stacked structure, although it can also be found in the less-stable *ABCABC* rhombohedral structure [7]. Here we consider only models involving the *ABAB* structure.

Under reactor-like conditions, the graphite is subjected to both heat and irradiation, resulting in defects within the lattice. Fast neutrons collide with the constituent carbon atoms, displacing them from their lattice sites, generating interstitial and vacancy defects. After irradiation, the interstitials are separated from the vacancies and it has been suggested that they can form clusters or 'platelets' between the layers in the graphite lattice [8–10]. If the platelet is sufficiently large, it produces a partial *C*-stacked layer, in order to reduce shear stress generated by *A* over *A* type stacking [9]. This is because the *AA* or *BB* stacking arrangement has the highest energy, which can be significantly reduced by adopting the *C* position. Thermalisation induces layer slippage and 'ripples' within the layers. With the increase in thermal energy, the atoms within the sample become able to vibrate, following Riley's theory [11], producing expansion in the *c*-direction ⟨0001⟩ and a slight contraction in the *a* direction over the temperature range 0 – 1000 K along with other physical effects [12–14].

The standard method for investigating the microstructure of graphite is through X-ray diffraction (XRD). Experimental analysis of XRD data is not trivial; the host of phenomenon that occur when graphite is placed under reactor conditions result in peaks that are often asymmetric and broad, which can be the result of many different variables (e.g., lattice spacing, stacking faults,

* Corresponding author.
E-mail addresses: R.Phillips3@lboro.ac.uk (R. Phillips), K.Jolley@lboro.ac.uk (K. Jolley), Y.Zhou4@lboro.ac.uk (Y. Zhou), R.Smith@lboro.ac.uk (R. Smith).

https://doi.org/10.1016/j.cartre.2021.100124

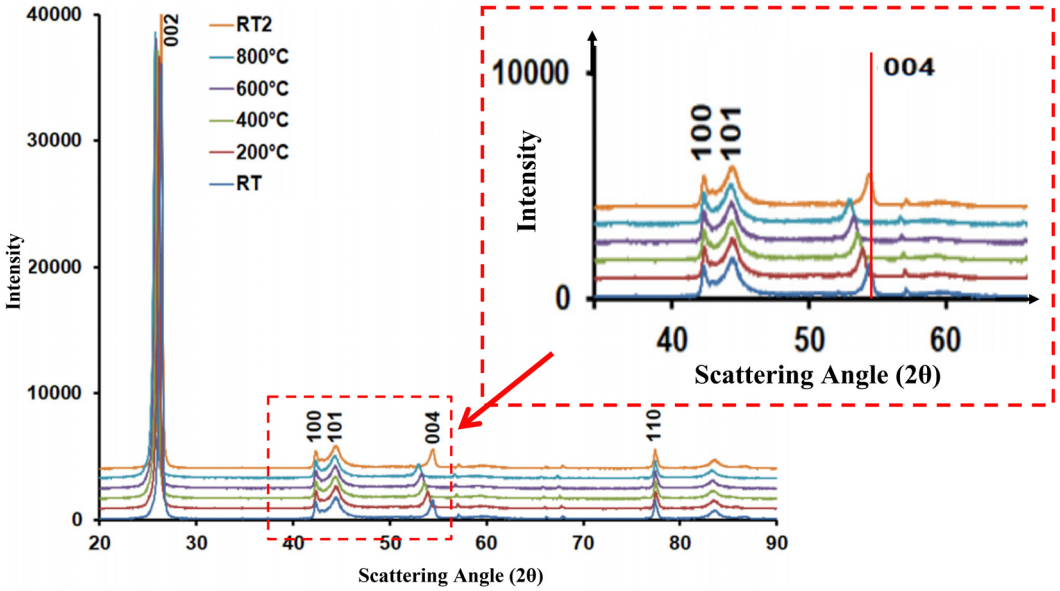

Fig. 1. Experimental literature powder XRD patterns for Sinosteel-produced SNG342 and SNG722 graphites at a range of temperatures. Image adapted from Ref[16]. Shifts are observed for the 00*l* peaks, with the 004 peak shift most easily visible. The shift of the 004 peak is highlighted by the inset showing a magnified section of the patterns. The dark blue and orange lines at the bottom and top respectively, show the XRD patterns acquired at room temperature. Data acquired at temperature increments of 200 °C are also shown. A red vertical line in the inset is included to mark the 004 peak and clearly highlights the shifting of this peak. (For interpretation of the references to colour in this figure legend, the reader is referred to the web version of this article.)

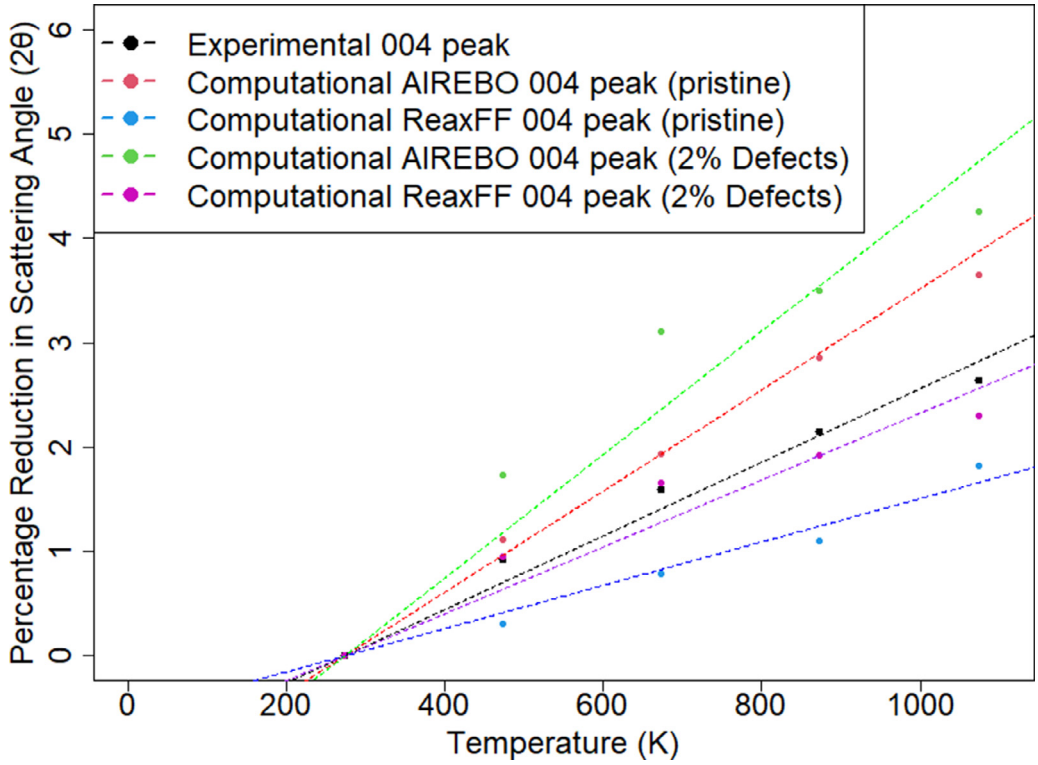

Fig. 2. A comparison between the percentage decrease in the scattering angle of the 004 peak with increasing temperature, for experimental and computational results. The defects line refers to 2% interstitials and vacancies randomly introduced.

point and extended defects, stresses or strain [1,5,15]). As such, the ability to determine the cause to changes in the XRD pattern of graphite is hindered. Recently, Hallam et al [16] have observed complex behaviour of SNG342 and SNG722 graphites. Their experimental powder XRD data has been reproduced in Fig. 1 with the shift of the 004 diffraction peak as a function of temperature highlighted by the magnified section.

Computationally characterising graphite has many advantages; effects within the system are able to be induced and analysed separately and their causes isolated, enabling for more accurate predictions in reactor-based scenarios.

The temperature influence on the XRD peaks of highly oriented pyrolytic graphite (HOPG) have also been investigated by other authors, for example, in [17,18] structural shifts of the 002 and 004

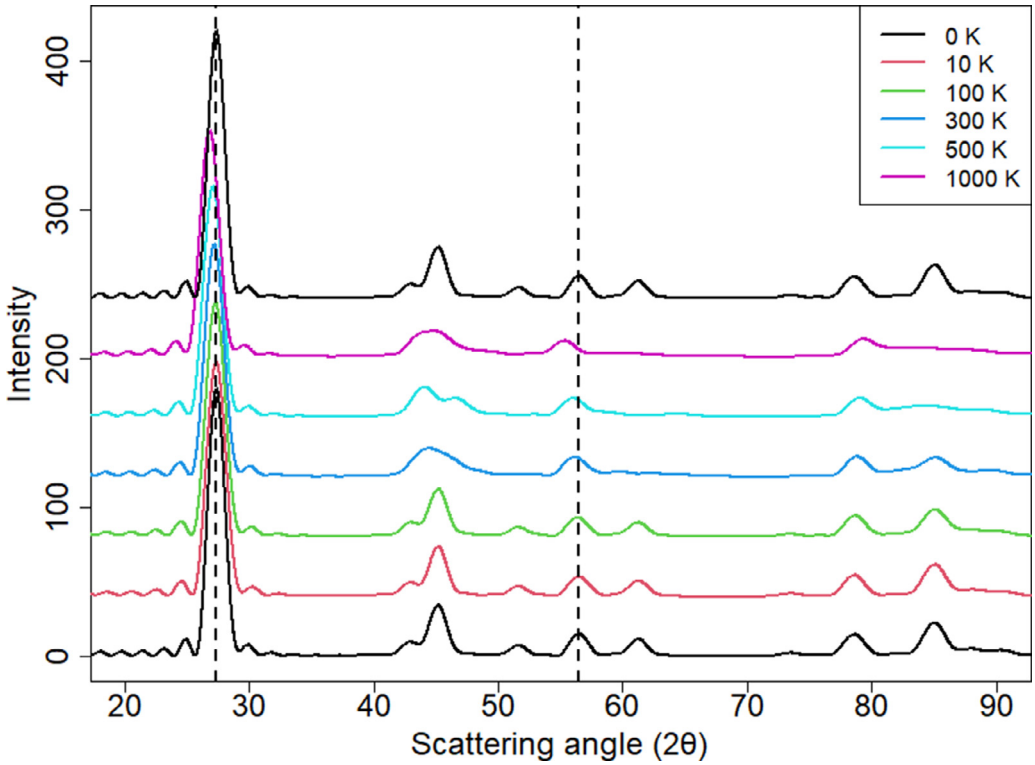

Fig. 3. Simulated XRD patterns for a 5 nm cube graphite crystal with *AB* stacking at temperatures of 10 K, 100 K, 300 K, 500 K and 1000 K. A shift in the 004 peak to lower angles is seen. A small shift in the 002 and 006/112 peaks is also observed. The peaks can also be seen to broaden and flatten with increasing temperature. The peaks are labelled, together with an interpretation in the figure in the Appendix.

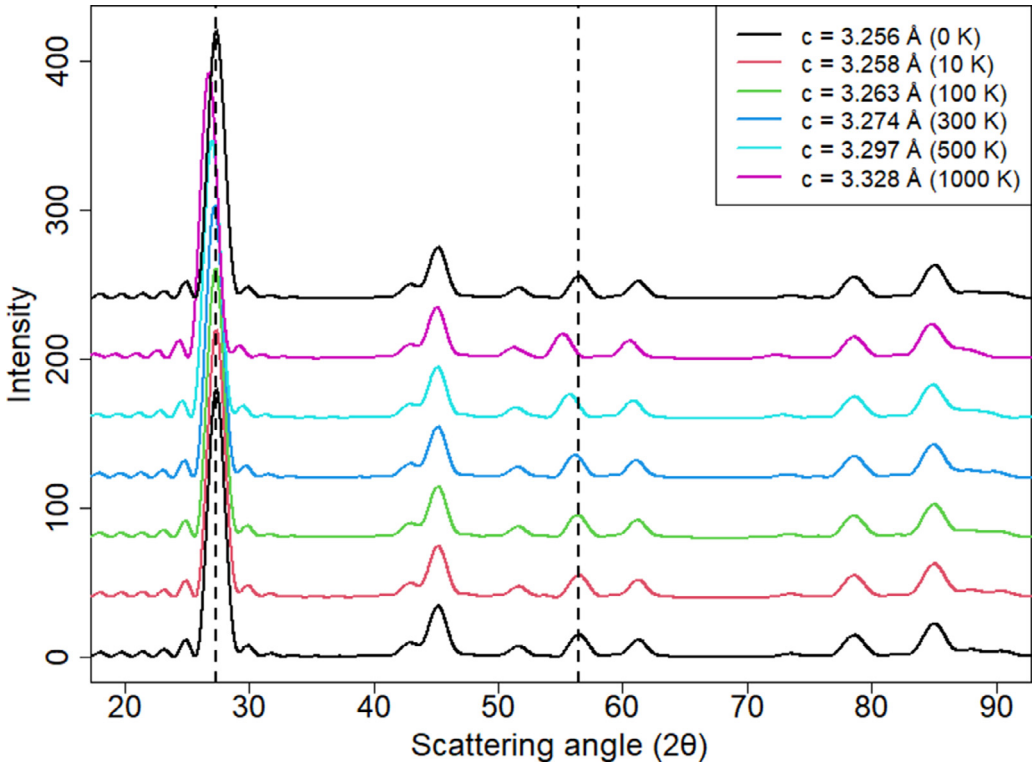

Fig. 4. XRD simulation results generated using the *c*-parameters in Table 1 at 0 K. The *a* parameter was kept constant at 2.4175 Å throughout. Signature peaks 00*l* (specifically at 002/ 26°, 004/ 55° and 006/87°) can be seen to shift to lower angles. A black trace is included at 26° and 55° for clarity.

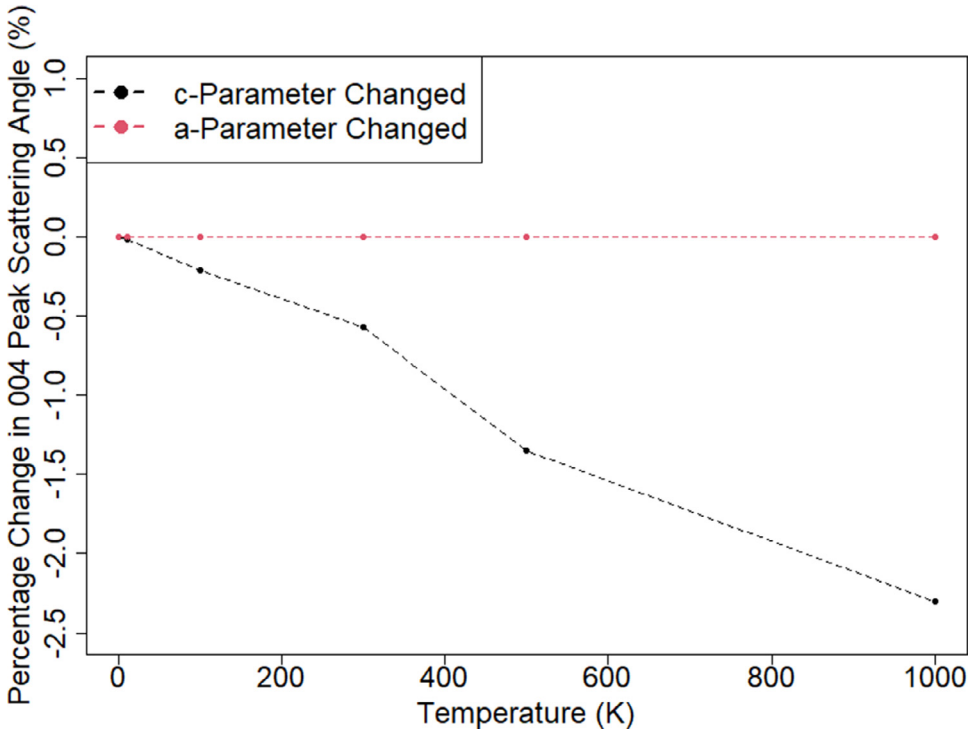

Fig. 5. A comparison between the percentage change in the 004 peak scattering angle generated by the change in *a* and *c* parameters as a function of temperature. The red curve corresponds to the 004 peaks found using XRD patterns generated using the *a* parameter values in Table 1 and the *c* parameter is kept constant. The black curve corresponds to the position of the 004 peak using the *c* parameter values from Table 1 with the *a* parameter being kept constant. (For interpretation of the references to colour in this figure legend, the reader is referred to the web version of this article.)

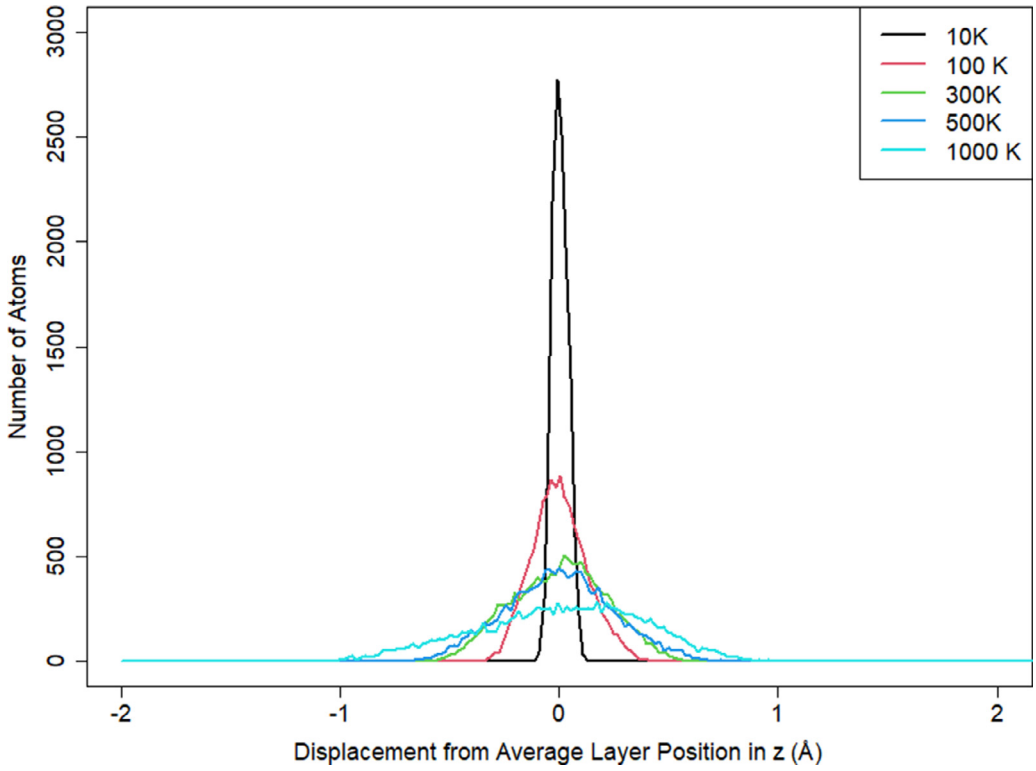

Fig. 6. The distribution of displacement of atoms in the *c* direction as a function of temperature in a system containing 14,112 atoms.

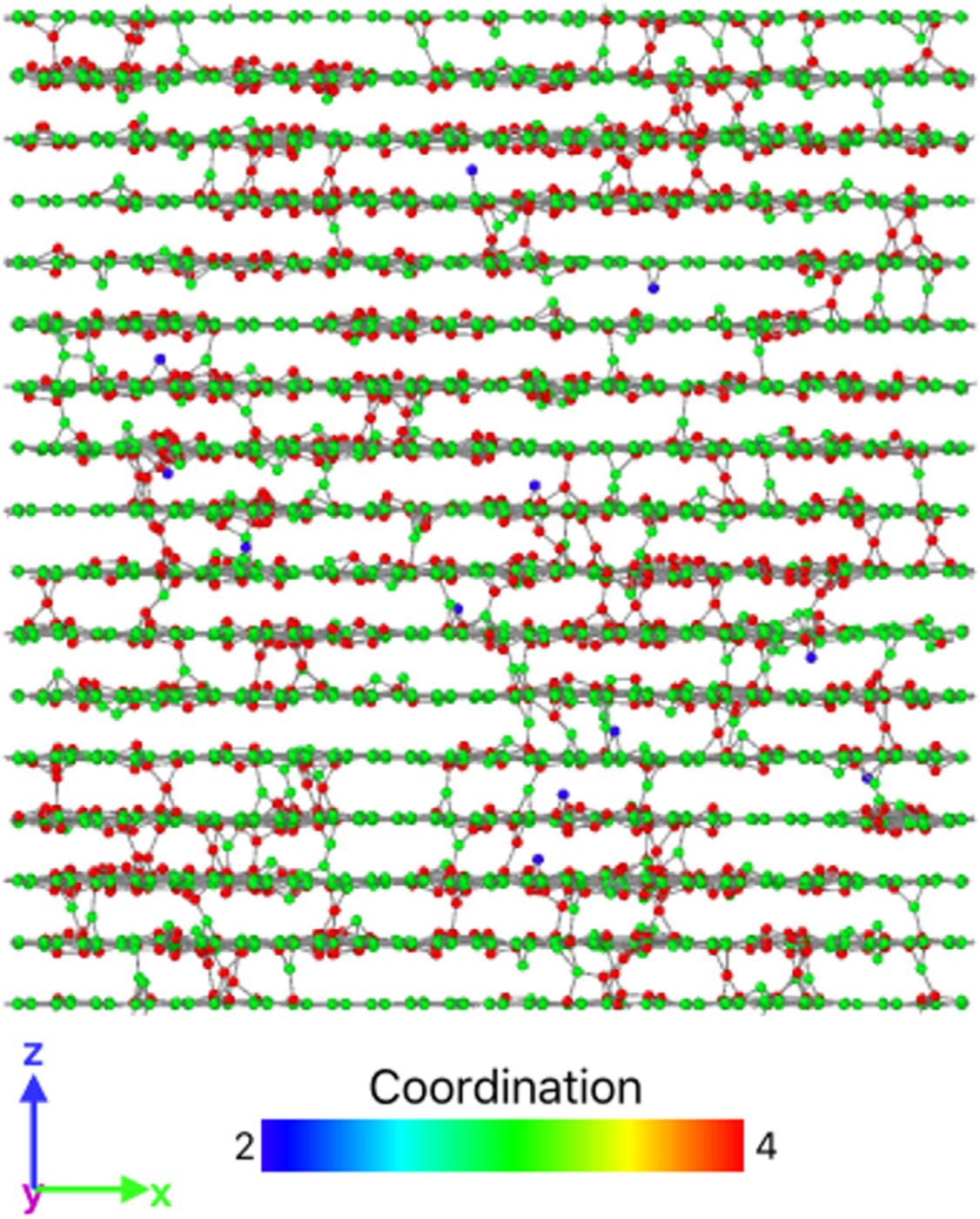

Fig. 7. A side view of the graphite lattice with 3% interstitials introduced. All atoms are coloured by coordination. Green coloured atoms denote a regular coordination of 3.

reflections of HOPG to lower angles, were investigated between 298 and 673 K. A corresponding increase in the *c* parameter was also noted which was much larger than previous measurements for turbostratic graphite.

Research has shown that for graphite, the 00*l* Powder X-Ray Diffraction peaks shift to lower angles with an increase in temperature, while the other signature peaks remain almost stationary [16]. Using computational methods, we are able to isolate the potential causes of this shift to lower angles and investigate them individually.

Similarly, it is possible to simulate defective graphite in order to ascertain the effects irradiation alone produces - effectively removing any undesirable interference due to the temperature factor on intensity. This allows the effects on XRD patterns of interstitial or vacancy defects to be observed separately. We are also able to exclude experimental complications such as the absorption of the X-rays within the material [15] since no X-rays are absorbed in our model whereas in a real experiment an empirical absorption factor is often used to account for X-ray absorption.

2. Methodology

Molecular Dynamics simulations were carried out using the LAMMPS [19] code. The interaction between the carbon atoms was

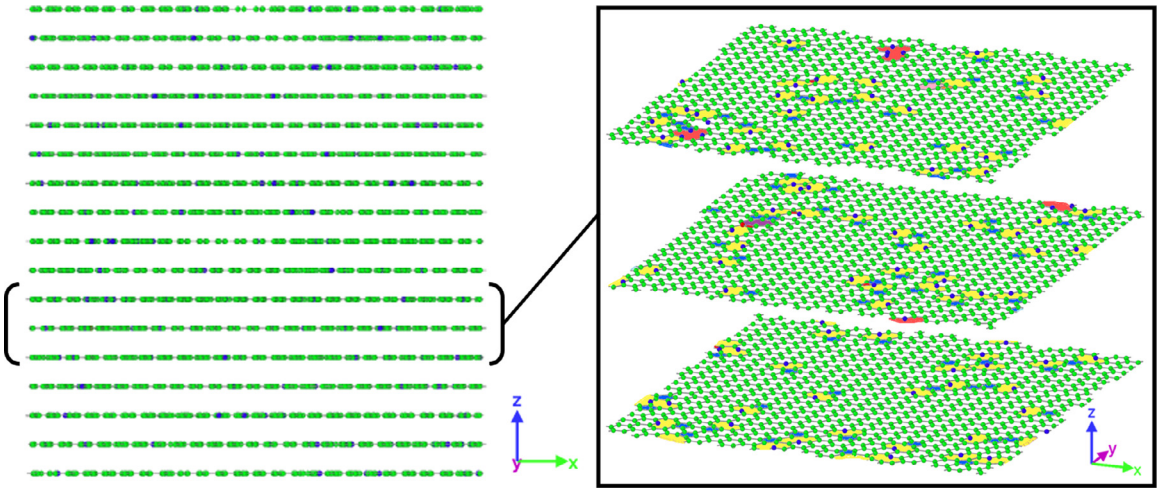

Fig. 8. Left: A side view of the graphite lattice with 3% vacancies introduced. Right: An exploded view of three of the individual layers that form the lattice. All atoms are coloured by coordination. Green coloured atoms denote a regular coordination of 3. Ring structures are coloured by number of atom members. Yellow-filled rings refer to 9 atoms loops, and blue refers to 5. Red filled loops have 3 atoms, pink have 7 and 'simple hole' structures are shown in orange. (For interpretation of the references to colour in this figure legend, the reader is referred to the web version of this article.)

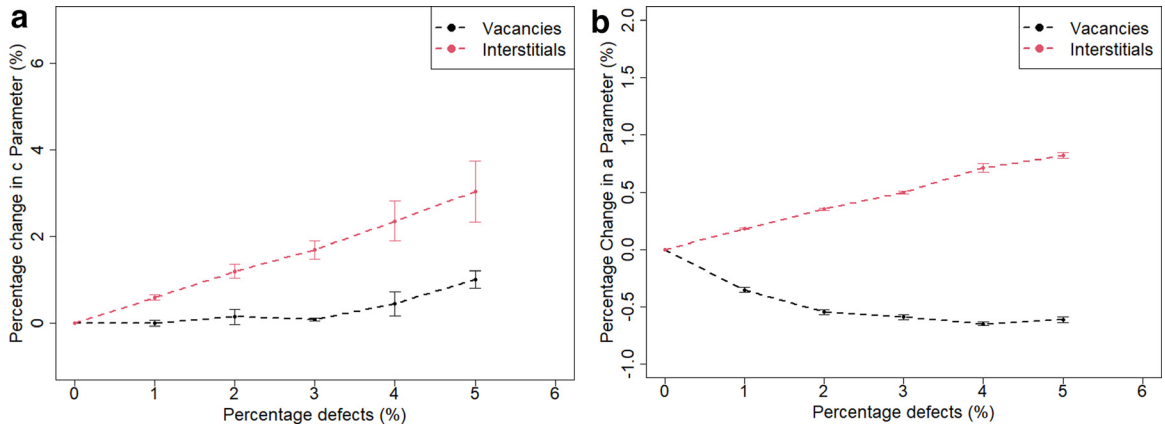

Fig. 9. A comparison of the *a* and *c* parameter changes when introducing vacancies or interstitials. (a) The *c* parameter change as a function of the number of vacancies (black) and interstitials (red) introduced. (b) The *a* parameter change as a function of the number of vacancies and interstitials introduced. (For interpretation of the references to colour in this figure legend, the reader is referred to the web version of this article.)

modelled using Molecular Dynamics with two different empirical potential formalisms: ReaxFF [20] and AIREBO [21]. Powder XRD patterns of the simulated structures were produced using the Debyer software [22]. The Debyer software has previously been used for investigating XRD patters in models of nuclear graphite by Chartier et al [23]. Diffraction patterns are produced based on the positions of atoms within a lattice, using Debye's scattering formula.

The ReaxFF potential parameters [20] were fitted to defect energies from Density Functional Theory (DFT) calculations using the AIMPRO code [24] and so models defect structures more accurately than some other empirical potentials but predicts slightly too large a value for the lattice parameters compared to experiment. Some simulations were also carried out using the AIREBO potential [21]. This gives good predictions of lattice parameters compared to experiment but is a poor fit for the energetics of defect structures [7,25,26].

The powder XRD analysis was simulated using an X-Ray wavelength of 1.540598 Å, which was chosen because the experimental XRD was obtained using a Cu κ_α radiation source. The diffraction profiles were obtained by varying the scattering angle (2θ) from 0° to 90° in a continuous scan mode with a step size of 0.01.

2.1. Thermalisation

A graphite cube consisting of 16,128 atoms arranged in *AB* stacking was generated using a Python script [27]. This produced a 5 nm cube with 16 layers and 1008 atoms per layer. The lattices were thermalised at temperatures of 10 K, 100 K, 300 K, 500 K or 1000 K for 16 ps until variations in the dimensions of the lattice were less than 0.05 Å, using a constant time step of 0.5 fs. The simulations were run in the isothermal-isobaric (NPT) ensemble with a Nose-Hoover thermostat. Once thermalised for 16 ps, a series of XRD patterns corresponding to the thermalisation temperatures were produced using Debyer.

2.2. Defect structures

Irradiation was modelled by the artificial introduction of interstitials and vacancies into the graphite lattices. Initially a 2% concentration of Frenkel pairs were introduced by randomly displacing 2% of the atoms within a perfect graphite lattice. The resulting structure was optimised using the conjugate gradient method. Lattices were prepared and optimised using both the AIREBO and ReaxFF models. The resulting XRD patterns at different temperatures were calculated using Debyer. Separately the effect of vacan-

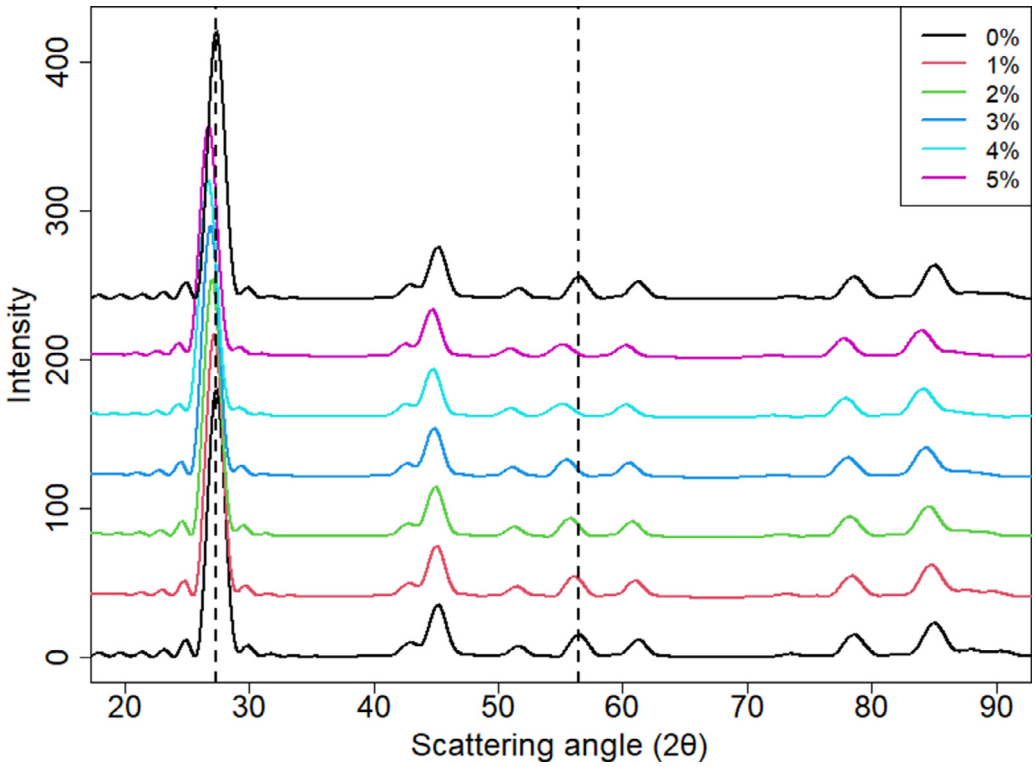

Fig. 10. Simulated powder XRD patterns of graphite with various percentages of interstitials using the ReaxFF model.

cies and interstitials were investigated using lattices prepared with the ReaxFF model only at 0 K.

In this latter case interstitials ranging in number up to 5% were introduced to random positions between the layers in the same sized lattice as used for thermalisation. After relaxation with the ReaxFF model, various interstitial defect structures were observed such as: the lowest energy 'spiro' defect, the y-lid, grafted and split interstitials ([28]). These lattices were then used to produce powder XRD patterns using Debyer. To overcome any effects due to the initial randomisation of the interstitial defects, the results were averaged over 15 different randomised configurations. Error bars are included in the plots. A similar number of structures were also examined for the vacancies. In the case of vacancies, a range of 0% - 5% of atoms were randomly removed and the system again relaxed. The introduction of vacancies caused only a small strain field around the vacancy with the layers remaining largely as arranged in the perfect defect-free structure.

3. Results and discussion

3.1. Effect of temperature

The reference lattice was heated to the specified temperatures using both the AIREBO and ReaxFF models. Once sufficiently thermalised, XRD patterns were produced from the output lattice. In Fig. 2 the percentage decrease in the scattering angle with increasing temperature is compared between computational and experimental results, with room temperature being the initial reference point in all cases. The scattering angle is seen to decrease for the 004 peak. Since the 004 peak is considerably broader than the 002 peak [29,30], and the experimental shifts with temperature are bigger [17] the 004 peak was chosen for investigation.

Both models (AIREBO and ReaxFF) do not match the experimental curve perfectly; ReaxFF predicts the percentage reduction to be lower than that seen experimentally while the AIREBO potential over-estimates the percentage reduction. The introduction of defects increases the shift in the peak, with ReaxFF predicting a curve much closer to experimental results.

The calculated powder XRD results obtained (Fig. 3) are similar to the experimental results in the literature [16] (Fig. 1) with an clear shift in the 004 peak towards lower angles. With increasing temperature, the peaks for these patterns broaden and flatten.

Heating of the graphite sample induces changes in the *a*-parameter, *c*-parameter and induces thermal vibrations in the position of the constituent atoms. After thermalisation and equilibration, the resultant lattice was used to find the lattice parameters for the corresponding temperature. These are displayed in Table 1.

In Table 1, we can see that only a small reduction occurs to *a*-parameter over the temperature range 0 – 1000 K which also does not produce any of the signature changes to the XRD pattern seen in Fig. 1 and is in agreement with the conclusions of Hallam et al. [16]. However the expansion in the *c*-parameter over this range of temperature is an order of magnitude greater. The predicted coefficient of thermal expansion (CTE) between 300 – 600 K in the *c*-direction, α_c, using the ReaxFF model [20] is about 20 $\times 10^{-6} K^{-1}$. This compares to experimental values of about 27 $\times 10^{-6} K^{-1}$ in Morgan's work [31] and 17 $\times 10^{-6} K^{-1}$ in the work of Boi et. al[17]. For the *a*-direction, Morgan [31] observed an initial contraction followed by expansion as the temperature is increased from about 70 K, with a minimum in the *a*-parameter occurring around 700 K. This effect is small with a minimum CTE of -1.3 $\times 10^{-6} K^{-1}$. In the classic work of Nelson and Riley [32] a qualitatively similar result is observed. The ReaxFF model also predicts a contraction followed by expansion in the *a*-direction, however, the effect is greater than that seen experimentally with a minimum CTE of about -4 $\times 10^{-6} K^{-1}$ and a minimum in the *a*-parameter occurring at about 1300 K. The AIREBO model predicts a monotonically increasing *a*-parameter with temperature with an average CTE of 1.6 $\times 10^{-6} K^{-1}$ over 0 – 1000 K.

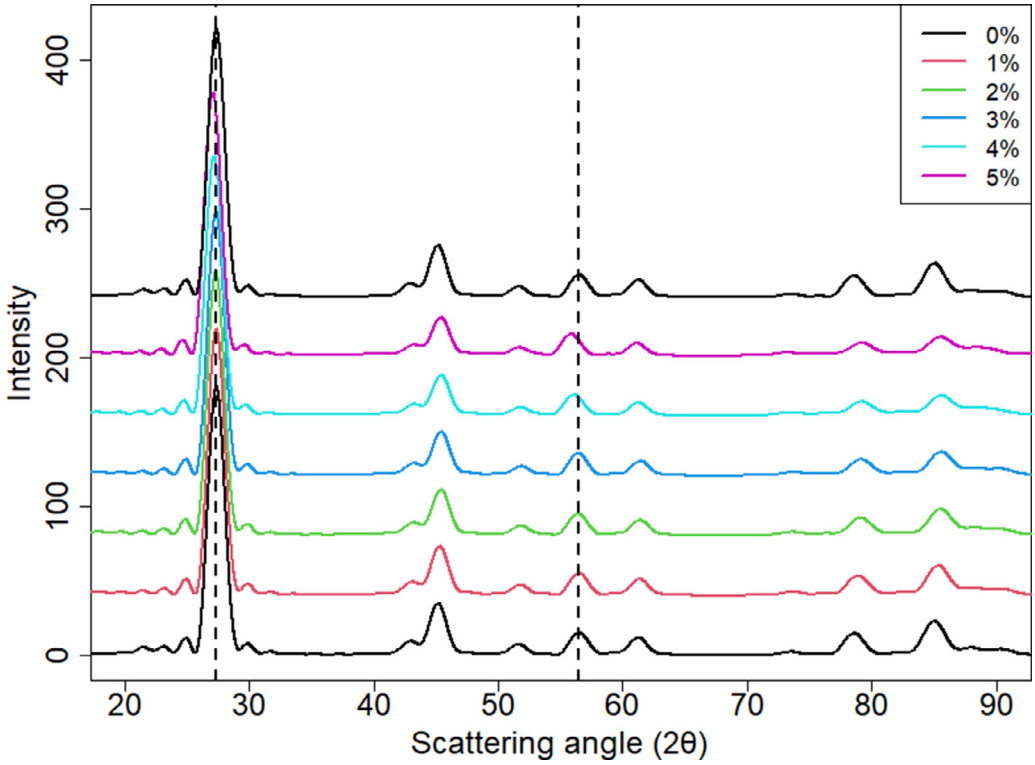

Fig. 11. Simulated powder XRD patterns of graphite at 0 K with various percentages of introduced vacancies.

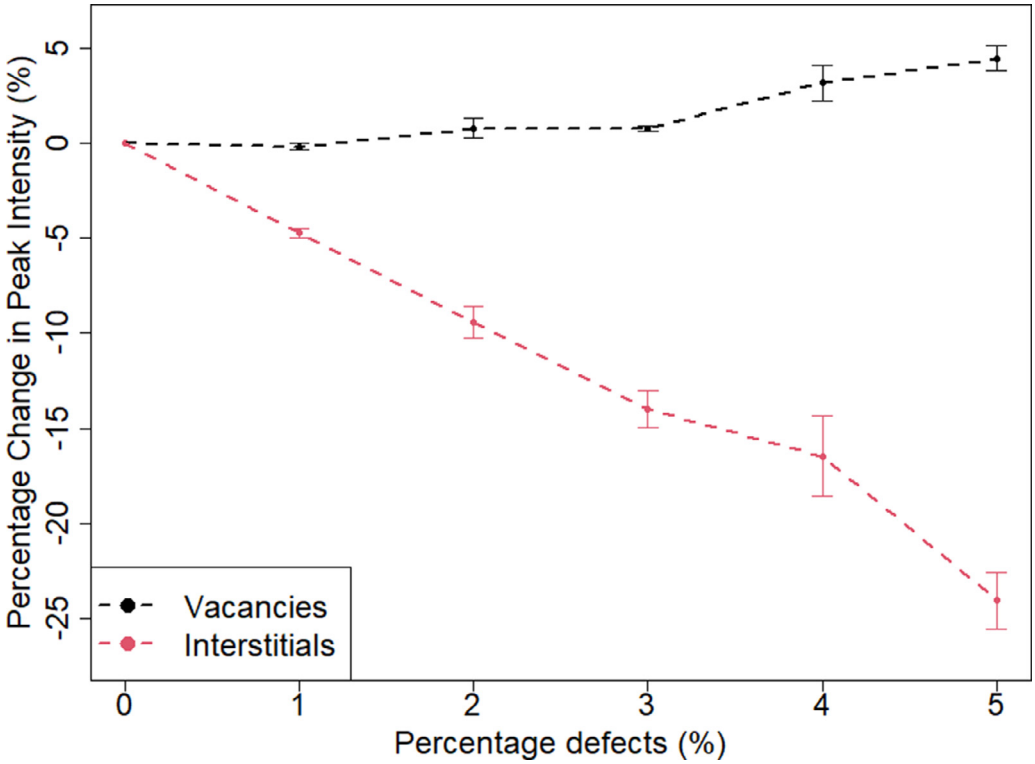

Fig. 12. The percentage reduction in the intensity of the 004 peak with varying levels of introduced defects. Vacancy defect concentrations are shown in black while interstitial defect concentrations are shown in red. (For interpretation of the references to colour in this figure legend, the reader is referred to the web version of this article.)

Table 1
The *a* and *c* lattice parameters of a 5 nm cube AB stacked graphite crystal for a range of temperatures calculated from the NPT simulations using the ReaxFF model. Values are an average over 16 ps of equilibration time.

Temperature (K)	*a*-parameter (Å)	*c*-parameter (Å)
0	2.433	3.256
10	2.432	3.258
100	2.432	3.263
300	2.430	3.274
500	2.429	3.297
1000	2.425	3.328

After obtaining the average *c*-parameters from NPT simulations at a range of temperatures, a new graphite lattice was generated with the python script with the appropriate *c*-parameter set corresponding to the temperature required. This effectively simply rescales the pristine zero K lattice in the ⟨0001⟩ direction while keeping the layers flat. These lattices were then used to produce the XRD patterns seen in Fig. 4.

In Fig. 4 the shift in the 004 peak can be clearly seen as would be expected with lattice expansion in the ⟨0001⟩ direction. Shifts to lower angles are also seen in the peaks at approximately 26° and 87°, corresponding to the 002 and 006 reflections. We also compared the percentage shift in the 004 peak while varying the *a* parameter (according to the values listed in Table 1) while keeping the *c* parameter fixed at 3.36 Å. Fig. 5 shows clearly that the variation of the *a* parameter has comparatively little effect on the 004 peak compared to the *c* parameter.

In Fig. 5 the direct effect of the *a* and *c* parameters on the scattering angle of the 004 peak can be seen. Using the *a* parameters from Table 1 while keeping *c* constant induces no significant change in the position of the 004 peak. However, changing *c* parameters using the values in Table 1 visibly induces a shift to lower angles in the 004 peak. Given that the peak shift to lower angles appears dependent on the *c*- parameter increase, it is logical to assume that any peak with an *l* component within the *hkl* indices might be affected.

These results are consistent with previous observations that XRD peak shifts to lower angles are are associated with induced strain [15,33].

There is no broadening of the peaks in Fig. 4 so it can be concluded that the *c* parameter expansion is not the source of this characteristic. Instead, it is expected that this is due to the vibration of atoms about their initial positions distorting the diffraction planes and lowering the intensity of reflecting X-rays. As temperature increases, the displacement from the average lattice layer position increases, as shown in Fig. 6. However no direct correlation between the displacement distributions and the change in intensity of the XRD peaks was observed.

From Fig. 6 the standard deviation of the spread of the vibrating atoms perpendicular to the graphene planes can be determined. Our values at 300 and 1000 K are roughly double than those obtained experimentally by Kellett and Jackets [34]. There are two possible explanations for this discrepancy. The graphite sample used by Kellett and Jackets was not pure with a *p* factor given by $p = .2$ (The *p* value gives a measure of how close a sample is to being pristine where $p = 0$ refers to perfect graphite [35]) and any interplanar spiro interstitial defects which are bonded to both planes and likely to be present in non-perfect graphite would reduce the vibrations. In addition the ReaxFF potential was not fitted to elastic properties.

3.2. Systems with point defects

Before simulating the XRD patterns of defective graphite the effect of introducing vacancies and interstitials on the structure of graphite was first examined. Here only the ReaxFF potential was used as this models defects more accurately than AIREBO.

Figs. 7 and 8 give visual representations of the state of the lattices after the separate introduction of 3% point defects. The effect on the *a* and *c* parameters as a function of the number of introduced defects is shown in Fig. 9.

Since the interstitials are all located between planes and the vacancies within the planes it would be expected that there would be expansion in the *c* direction in the case of interstitials and contraction in the *a* direction as quantified in Fig. 9.

The results on dimensional change are not completely comparable to experimental results. In a review of work up to the mid 1960/s Kelly et al [36] observed contraction of pile grade A (PGA) nuclear graphite in the temperature range 0 – 650 °C after neutron irradiation up to quite high doses ($4 \times 10^{21}/cm^2$) whereas Texas coke graphite showed an expansion. In a later study Koike and Pedraza [37] showed experimentally that after irradiation, HOPG underwent an expansion in the *c* direction and a contraction in the *a* direction. In Fig. 9 contraction in the *a* direction only occurs due to the presence of vacancies. In [23] a comparison is made between experimental measurements of dimensional change carried out in both [38] and [37] and MD simulations with a different potential model to ours with up to 25% defects. Their MD simulation overestimate the swelling compared to experiment giving about 5% expansion of the *c* parameter at 5% defect concentration compared to about 3.75% experimentally. Our results are not directly comparable as we have separated out the effects of vacancies and interstitials, but it appears that the ReaxFF model gives lower values for the *c* expansion than the model used in [23].

XRD patterns are simulated at 0 K for systems with various percentages of introduced defects.

For the case of interstitials as shown in Fig. 10, it can be seen that all the peaks match with the signature diffraction lines for graphite as in Fig. A.14. Introducing interstitial atoms into the graphite lattice results in a broadening of the XRD peaks and a reduction in intensity. This occurs for all peaks but is visibly more pronounced for 00*l* peaks.

In Fig. 11, broadening of the XRD peaks is minimal. As per Fig. 12, the percentage broadening/intensity reduction is considerably less than the corresponding interstitial case. Images of the defective lattices, Figs. 7 and 8, clearly show that reflecting planes are preserved more clearly after the introduction of vacancies. In contrast with the introduction of interstitials, significant peak broadening and loss of intensity is observed for all signature peaks, not only 00*l* peaks.

From Fig. 12, we can see that as the percentage of interstitials increases, the intensity of the 004 peak decreases. This corresponds directly with the increasing level of disorder within the sample.

As in similar experimental studies [39], there is a shift to lower angles of peaks that correspond to the 00*l* index [5,40]. This can be seen clearly in Fig. 13. Fig. 9 shows that the average *c* parameter increases with the number of added interstitials until 5% where it is 0.18 Å larger than at 0% concentration. In contrast the *a* parameter remains almost constant, with a change of 0.017 Å between 0% and 5% interstitial concentration.

In Fig. 11, there is a small shift to lower angles for the 004 peak, possibly due to the strain induced by the increase in interlayer disorder. Fig. 13, shows that the introduction of vacancies and interstitials results in the 004 peak shifting to lower angles. However, the introduction of interstitials causes the 004 peak to shift a greater amount compared to vacancies. Other peaks experience

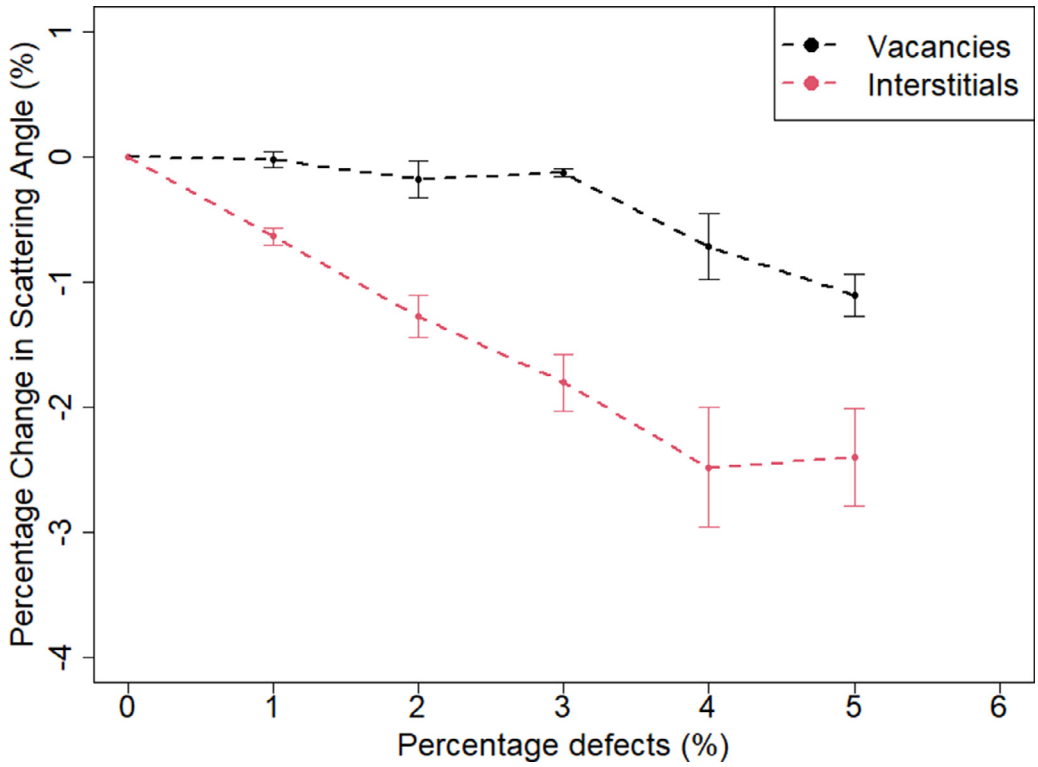

Fig. 13. The percentage change in the scattering angle of the 004 peak with varying levels of defects introduced. The black curve refers to the introduction of vacancies while the red curve refers to the introduction of interstitials. (For interpretation of the references to colour in this figure legend, the reader is referred to the web version of this article.)

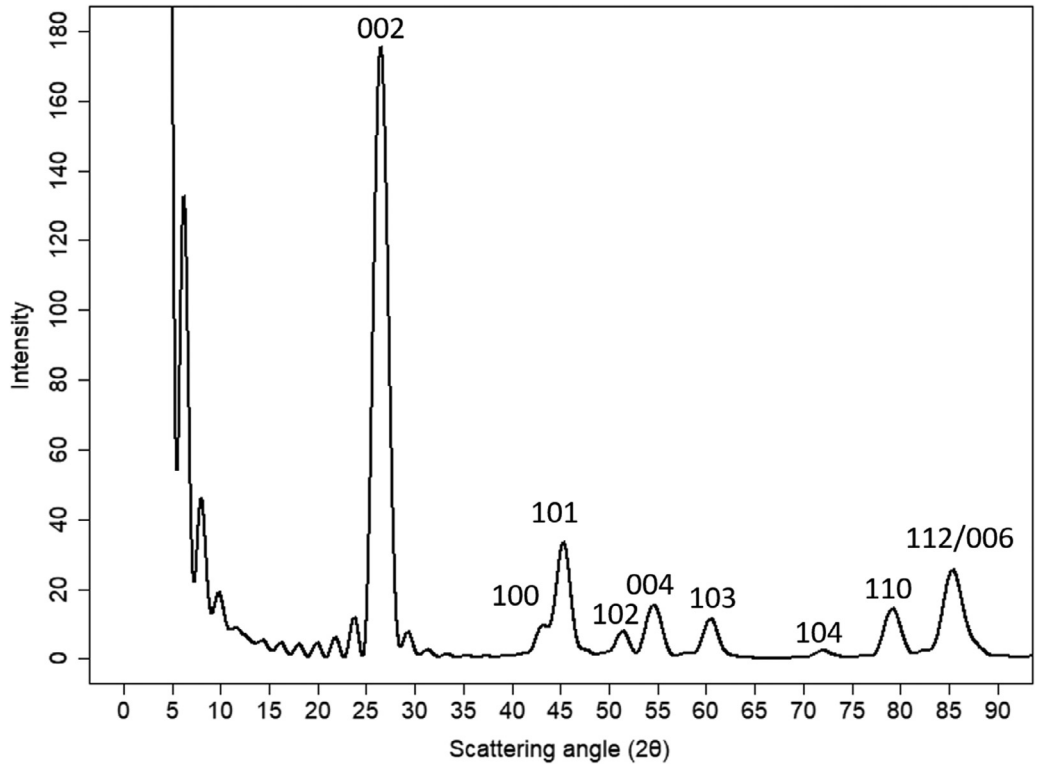

Fig. A.14. A simulated XRD pattern of perfect *AB* stacked graphite at 0K. The simulated diffraction lines are in good agreement with those produced from experiments [5,41,42]. Due to the layer stacking in graphite, the material is highly anisotropic. Thus the diffraction lines are classified into three groups; lines with 00*l*, *hk*0, and *hkl* indices [41]. 00*l* diffraction lines are produced by reflections between basal planes where destructive interference prevents odd-numbered 00*l* indices. *hk*0 diffraction lines are produced by reflections from crystallographic planes perpendicular to the basal plane. *hkl* reflections arise as property of regular stacking of layers [42]. Due to closeness of peaks, the 006 peak is not distinguishable from the 112 peak.

a shift to greater angles due to the compression in the in-plane direction.

4. Conclusions

Simulated XRD patterns have been produced both by lattice heating and by the introduction of defects. X-Ray diffraction patterns show that interlayer lattice spacing increase is the cause of signature 00*l* peaks shifting to lower angles, whether that increase is due to the heating of the graphite or the generation of interplanar interstitial atoms which push apart the lattice planes. Peak broadening and the loss of intensity is due to the movement of atoms away from the pristine diffracting planes, whether that displacement is caused via thermal vibrations or through the expulsion of atoms from their lattice sites.

Heating of the graphite sample has been shown to induce an expansion in the *c* spacing of the lattice with minimal effects on the *a* parameter, in agreement with similar experiments [16]. This directly results in a peak shift of 00*l* peaks to lower angles with no movement of any intra-layer peak reflections.

Even relatively low levels of interstitial atoms within the graphite can result in a significant reduction in intensity of the 00*l* peaks. The level of intensity reduction for all signature peaks is dependent on the whether in-plane or inter-plane reflections generate the peak itself - with in-plane reflections being less affected - and how well the reflection planes in those directions are maintained. Interstitials also cause a small shift in all peaks to lower angles, as strain is induced in both the interlayer and intralayer directions.

In the case of vacancies, broadening and loss of intensity is experienced at all peaks due to the vacancies disrupting the hexagonal formation of the planes. The level of broadening and intensity loss for the 004 peak is consistently less than when introducing interstitials. Unlike with interstitials, non-00*l* peaks experience a small shift to higher scattering angles due to intra-layer shrinkage.

It is clear from this work that the effect of the microstructure on the XRD patterns is significant. This is effect is clearly seen in the single crystal structures with vacancy and interstitial defects, and a simple layer expansion model can explain the shifting of the XRD peaks observed by experimental researchers. In future it would be advantageous to perform a wider study of the effects of other point and extended defect structures, and to model more complex atomistic lattices that are more representative of real nuclear graphite grades. A suggestion is to investigate the effects of basal and prismatic defects and nano-onion and nanotube inclusions. The methods used here could enable the changes experienced by graphite under reactor-like conditions to be quantified, leading to a better understanding of the modification of the physical properties.

Declaration of Competing Interest

All authors declare they have no known cause for bias in the work presented in this paper.

Acknowledgment

The authors thank Loughborough University for providing funding for this work and Dr Peter Flewitt of Bristol University for helpful discussions and interesting insights. Additionally Kenny Jolley gratefully acknowledges funding from EDF 2016–2021.

Appendix A

References

[1] Z. Zhou, W. Bouwman, H. Schut, C. Pappas, Interpretation of x-ray diffraction patterns of (nuclear) graphite, Carbon N Y 69 (2014) 17–24, doi:10.1016/j.carbon.2013.11.032.
[2] A. Wickham, B. Marsden, Characterisation, Treatment and Conditioning of Radioactive Graphite from Decommissioning of Nuclear Reactors, IAEA TEC-DOC-1521, 2006.
[3] J. Steinbeck, G. Braunstein, M. Dresselhaus, T. Venkatesan, D. Jacobson, A model for pulsed laser melting of graphite, J Appl Phys 58 (11) (1985) 4374–4382.
[4] F. Bundy, Melting of graphite at very high pressure, J Chem Phys 38 (3) (1963) 618–630.
[5] Z. Zhou, W. Bouwman, H. Schut, T. van Staveren, M. Heijna, C. Pappas, Influence of neutron irradiation on the microstructure of nuclear graphite: an x-ray diffraction study, J. Nucl. Mater. 487 (2017) 323–330, doi:10.1016/j.jnucmat.2017.02.004.
[6] H. Freeman, A. Jones, M. Ward, F. Hage, N. Tzelepi, Q. Ramasse, A. Scott, R. Brydson, On the nature of cracks and voids in nuclear graphite, Carbon N Y 103 (2016) 45–55, doi:10.1016/j.carbon.2016.03.011.
[7] S.K. Pregler, T. Hayakawa, H. Yasumatsu, T. Kondow, S.B. Sinnott, Combined computational and experimental study of ar beam induced defect formation in graphite, Nucl. Instrum. Methods Phys. Res., Sect. B 262 (2) (2007) 240–248, doi:10.1016/j.nimb.2007.05.030.
[8] Y. Zhou, K. Jolley, R. Phillips, R. Smith, H. Wu, Modelling defect evolution in irradiated graphite, Carbon N Y 154 (2019) 192–202, doi:10.1016/j.carbon.2019.07.092.
[9] W. Reynolds, Physical Properties of Graphite, Elsevier Materials Science Series, Elsevier Publishing Company, 1969.
[10] G.W. Hinman, A. Haubold, J. Gardner, J.K. Layton, Vacancies and interstitial clusters in irradiated graphite, Carbon N Y 8 (3) (1970) 341–351, doi:10.1016/0008-6223(70)90074-6.
[11] D. Riley, The thermal expansion of graphite: part ii. theoretical, Proceedings of the Physical Society (1926–1948) 57 (6) (1945) 486.
[12] B.J. Marsden, M. Haverty, W. Bodel, G. Hall, A. Jones, P. Mummery, M. Treifi, Dimensional change, irradiation creep and thermal/mechanical property changes in nuclear graphite, Int. Mater. Rev. 61 (3) (2016) 155–182.
[13] W. Morgan, Thermal expansion coefficients of graphite crystals, Carbon N Y 10 (1) (1972) 73–79.
[14] P.J. Hacker, G.B. Neighbour, B. McEnaney, The coefficient of thermal expansion of nuclear graphite with increasing thermal oxidation, J Phys D Appl Phys 33 (8) (2000) 991.
[15] B.D. Cullity, Elements of X-ray diffraction, 2nd, Addison-Wesley, 2001.
[16] K.R. Hallam, J.E. Darnbrough, C. Paraskevoulakos, P.J. Heard, T.J. Marrow, P.E. Flewitt, Measurements by x-ray diffraction of the temperature dependence of lattice parameter and crystallite size for isostatically-pressed graphite, Carbon Trends (2021) 100071.
[17] F.S. Boi, M. Liu, J. Xia, O. Odunmbaku, A. Taallah, J. Wen, Temperature driven anomalous unit-cell c-axis shifts in highly oriented pyrolytic graphite measured at the magic-angle, Carbon N Y 145 (2019) 690–693.
[18] F.S. Boi, M. Liu, J. Xia, O. Odunmbaku, A. Taallah, J. Wen, Anomalous c-axis shifts and symmetry enhancement in highly oriented pyrolytic graphite at the magic angle, Carbon N Y 150 (2019) 27–31.
[19] S. Plimpton, Fast parallel algorithms for short-range molecular dynamics, J. Comput. Phys. 117 (1) (1995) 1–19, doi:10.1006/jcph.1995.1039. URL: http://lammps.sandia.gov
[20] R. Smith, K. Jolley, C. Latham, M. Heggie, A. Van Duin, D. van Duin, H. Wu, A reaxff carbon potential for radiation damage studies, Nucl. Instrum. Methods Phys. Res. B 393 (2017) 49–53.
[21] D.W. Brenner, O.A. Shenderova, J.A. Harrison, S.J. Stuart, B. Ni, S.B. Sinnott, A second-generation reactive empirical bond order (REBO) potential energy expression for hydrocarbons, J. Phys. - Condens. Mat. 14 (4) (2002) 783–802, doi:10.1088/0953-8984/14/4/312.
[22] M. Wojdyr, 2011, https://github.com/wojdyr/debyer, documentation: https://debyer.readthedocs.io/en/latest/#.
[23] A. Chartier, L. Van Brutzel, J. Pageot, Irradiation damage in nuclear graphite at the atomic scale, Carbon N Y 133 (2018) 1224–1231.
[24] R. Jones, P. Briddon, The ab initio cluster method and the dynamics of defects in semiconductors, Semiconductors and Semimetals 51 (1998) 287–349.
[25] T. Trevethan, M. Heggie, Molecular dynamics simulations of irradiation defects in graphite: single crystal mechanical and thermal properties, Comput. Mater. Sci 113 (2016) 60–65, doi:10.1016/j.commatsci.2015.11.012.
[26] B. Farbos, H. Freeman, T. Hardcastle, J.-P. Da Costa, R. Brydson, A.J. Scott, P. Weisbecker, C. Germain, G.L. Vignoles, J.M. Leyssale, A time-dependent atomistic reconstruction of severe irradiation damage and associated property changes in nuclear graphite, Carbon N Y 120 (2017) 111–120, doi:10.1016/j.carbon.2017.05.009.
[27] K. Jolley. https://github.com/Kenny-Jolley/LAMMPS_UTILITIES.
[28] C. Latham, A. McKenna, T. Trevethan, M. Heggie, M. Rayson, P. Briddon, On the validity of empirical potentials for simulating radiation damage in graphite: a benchmark, J. Phys. Condensed Matter 27 (2015) 316301.
[29] R.E. Franklin, The interpretation of diffuse x-ray diagrams of carbon, Acta Crystallogr 3 (2) (1950) 107–121.

[30] R.E. Franklin, The structure of graphitic carbons, Acta Crystallogr 4 (3) (1951) 253–261.
[31] W. Morgan, Thermal expansion coefficients of graphite crystals, Carbon N Y 10 (1) (1972) 73–79, doi:10.1016/0008-6223(72)90011-5.
[32] J. Nelson, D. Riley, The thermal expansion of graphite from 15°c to 800°c : part i. experimental, Proc. Phys. Soc. 57 (1945) 477–486.
[33] G. Tutuncu, Analysis and interpretation of diffraction data from complex, anisotropic materials (2010).
[34] E. Kellett, B. Jackets, B. Richards, A study of the amplitude of vibration of carbon atoms in the graphite structure, Carbon N Y 2 (2) (1964) 175–183.
[35] E. Kellett, B. Richards, The thermal expansion of graphite within the layer planes, J. Nucl. Mater. 12 (2) (1964) 184–192.
[36] B. Kelly, W. Martin, P. Nettley, Dimensional changes in polycrystalline graphites under fast-neutron irradiation, Philosophical Transactions of the Royal Society of London. Series A. Mathematical and Physical Sciences 260 (1109) (1966) 37–71.
[37] J. Koike, D.F. Pedraza, Dimensional changes in highly oriented pyrolytic graphite due to electron-irradiation, J Mater Res 9 (7) (1994) 1899–1907.
[38] H. Freeman, A. Scott, R. Brydson, Thermal annealing of nuclear graphite during in-situ electron irradiation, Carbon N Y 115 (2017) 659–664.
[39] P.F.A. el Turke, et al., X-ray diffraction analysis - role of temperature and neutron irradiation, 2018,
[40] R. Krishna, J. Wade, A.N. Jones, M. Lasithiotakis, P.M. Mummery, B.J. Marsden, An understanding of lattice strain, defects and disorder in nuclear graphite, Carbon N Y 124 (2017) 314–333, doi:10.1016/j.carbon.2017.08.070.
[41] M. Inagaki, Chapter 2.1 - advanced carbon materials, Elsevier Inc., 2013, pp. 25–60, doi:10.1016/B978-0-12-385469-8.00002-2.
[42] K. Jurkiewicz, M. Pawlyta, A. Burian, Structure of carbon materials explored by local transmission electron microscopy and global powder diffraction probes, C-Journal of Carbon Research 68 (4) (2018).